Final Draft
of the original manuscript:

Christiansen, M.B.; Koch, W.; Horstmann, H.; Hasager, C.B.; Nielsen, M.:
Wind resource assessment from C-band SAR
In: Remote Sensing of Environment (2006) Elsevier

DOI: 10.1016/j.rse.2006.06.005

Editorial Manager(tm) for Remote Sensing of Environment
Manuscript Draft

Manuscript Number:

Title: Wind resource assessment from C-band SAR: optimizing the data input

Article Type: Full length article

Section/Category:

Keywords: Synthetic aperture radar, ERS-2, Envisat, geophysical model function, local gradient, wind mapping, wind resource assessment, wind energy

Corresponding Author: Ms. Merete Bruun Christiansen, M.Sc.

Corresponding Author's Institution: Risø National Laboratory

First Author: Merete Bruun Christiansen, M.Sc.

Order of Authors: Merete Bruun Christiansen, M.Sc.; Wolfgang Koch; Jochen Horstmann; Charlotte Bay Hasager; Morten Nielsen

Manuscript Region of Origin:

Abstract:

Abstract

Wind fields retrieved from high-resolution synthetic aperture radar (SAR) images are valuable in wind resource assessment offshore. In contrast to in situ measurements, SAR wind maps provide spatial information which allows wind farm developers to compare the wind resource for different sites. Further advantages include the opportunity to obtain archived data and a low cost of satellite based assessments compared to the cost of installing a meteorological mast offshore. Using accurate inputs of wind speed is crucial in wind resource assessment, as predicted power is proportional to the wind speed cubed. Wind speeds retrieved from a series of 97 high-resolution ERS-2 SAR and Envisat ASAR images, at moderate wind speeds (2-15 m s^{-1}), were validated against in situ measurements from an offshore mast in the North Sea. The wind direction input, necessary for SAR wind speed retrievals, was obtained from the meteorological mast and from a local gradient analysis of streaks in the SAR images. For the first method, a standard deviation of ~1.1 m s^{-1} was found. The second method, which worked independently of in situ measurements, yielded a standard deviation of ~1.3 m s^{-1}. The performance of three geophysical model functions was compared. The best approximation to the in situ measurements of wind speed was found for CMOD-IFR2, despite a bias on the order of -0.3 m s^{-1}. CMOD4 retrievals also underestimated the wind speed, whereas the bias on CMOD5 retrievals was negligible. The accuracy on SAR wind retrievals improved as cases with a long fetch and near-neutral atmospheric stability were analyzed separately. The mean wind speed, obtained from the 97 SAR scenes, was linked closely to the bias on SAR wind retrievals. Agreement to ±15% of the in situ measurements was found for all the wind retrieval methods tested. The

accuracy on power density estimates, on the other hand, was determined by the standard deviation of SAR wind retrievals relative to the in situ measurements. SAR wind fields retrieved with CMOD-IFR2, using in situ wind direction inputs, yielded exactly the power density predicted from in situ measurements alone. Predictions of the wind resource from SAR measurements corresponded well to predictions from longer time series of in situ measurements. This indicates that a reliable wind resource assessment may be achieved from a series of randomly selected SAR images. The findings presented here could be useful in future wind resource assessment based on SAR images.

1. Introduction

Finding the optimum wind resource is crucial in the planning of new wind farms, as the wind climate determines the energy production. The mean power density, E [W m^{-2}] of the wind is given by:

$$E = \frac{1}{2} \rho U^3 \quad (1)$$

where ρ [kg m^{-2}] is the air density and U [m s^{-1}] is the mean wind speed. Accurate estimates of the mean wind speed are thus vital for a reliable wind power prediction (Troen & Petersen, 1989).

Wind maps retrieved from synthetic aperture radar (SAR) data have proven useful in offshore wind resource assessment (Choisnard et al., 2004; Hasager et al., 2005; Schneiderhan et al., 2005). SAR wind maps provide high-resolution spatial information, which cannot be gathered from meteorological measurements. Further advantages include the low cost of SAR images, compared to the cost of installing and operating an offshore meteorological mast, and the opportunity to obtain archived data. The high accuracy of modern meteorological measurements cannot be achieved with a SAR. Hence, using SAR data is most viable in the early stage of wind farm siting, before in situ measurements are available. In this paper, we address the application of SAR data in wind resource assessment.

SAR is an active microwave remote sensing technique. The radar signal emitted from a SAR is partly returned from the Earth surface through Bragg scattering. The backscattering depends on surface roughness elements comparable in size to the radar wavelength. Here we are concerned with wind retrievals offshore from the C-band (5.3 GHz) SAR sensors on board the ERS-2 and Envisat satellites operated by the European Space Agency (ESA). The polar-orbiting satellites were launched in 1995 and 2002, respectively, and both are presently in orbit. The principle of C-band SAR wind retrieval is that the wind generates small scale roughness at the sea surface in the form of capillary-gravity waves. The instant wind is proportional to the returned radar signal per area, which is the normalized radar cross section, NRCS.

Geophysical model functions (GMFs) have been developed to empirically identify the relationship of wind speed at 10 m to NRCS, which depends on the wind direction relative to the radar look direction and on the radar incidence angle. A series of GMFs known as the CMOD functions were originally developed for global coverage scatterometer wind retrievals in C-band (Hersbach, 2003; Quilfen et al., 1998; Stoffelen & Anderson, 1997). Later, the CMOD functions have been successfully applied to wind retrievals from high-resolution SAR images; a review is provided by Monaldo & Kerbaol (2003). The CMOD functions apply to SAR data acquired with vertical polarization but it is possible to account for the lower NRCS of horizontally polarized SAR data through multiplication with a polarization ratio e.g. Thompson et al. (1998).

Scatterometers are capable of acquiring multiple NRCS images simultaneously, which allows determination of both wind speed and direction. SAR images, in contrast, are

acquired with a single look angle such that several wind speed and direction pairs correspond to a given NRCS. It is therefore necessary to know the wind direction a priori in order to determine the wind speed. Wind directions may be obtained from atmospheric models (Monaldo, 2000; Monaldo et al., 2001), scatterometry (He et al., 2005; Monaldo et al., 2004), or in situ measurements (Hasager et al., 2004). In addition, it is possible to extract the wind direction from streaks in the SAR images. The streaks originate from roll vortices aligned approximately with the wind direction. Methods to determine the streak direction include FFT (Furevik et al., 2002; Gerling, 1986; Lehner et al., 1998), wavelet analysis (Du et al., 2002; Fichaux & Ranchin, 2002) and local gradients (Horstmann et al., 2002a; Koch, 2004). The 180° ambiguity associated with these methods may be removed through comparison with other data sources or through a study of wind shadows in the images. There is usually a trade-off between the accuracy of wind direction estimates and the degree of automation in the process of determining the directions. In situ measurements and image streaks have the advantage of being correlated in time with satellite overpasses, and are therefore particularly attractive data sources.

Wind speeds of 2-24 m s^{-1} can be retrieved with the nominal accuracy ±2 m s^{-1} for radar incidence angles of 20-60° using the scatterometer approach (Stoffelen & Anderson, 1997). The approach applies to open oceans and validation studies have shown that ocean winds retrieved from high-resolution SAR correspond well to scatterometer measurements (Horstmann et al., 2003; Monaldo et al., 2004). High-resolution SAR wind retrievals have also been evaluated for near-shore areas. Monaldo et al. (2001) found a standard deviation of 1.8 m s^{-1} for comparisons of horizontally polarized

RADARSAT wind retrievals to buoy measurements along the US east coast using CMOD4. Furevik et al. (2002) compared ERS-2 SAR wind retrievals along the marginal ice zone of Svalbard to measurements from ships. They found an rms error of 1.6 m s^{-1} using CMOD-IFR2 and a larger rms error for CMOD4. Hasager et al. (2004) validated CMOD-IFR2 and CMOD4 wind retrievals against measurements from an offshore meteorological mast in the North Sea. A standard error of 0.9 m s^{-1} was found for CMOD4 wind retrievals using in situ wind direction inputs. The same GMF used with FFT-derived wind directions resulted in a standard error of 1.3 m s^{-1}. The most recent GMF is CMOD5, which was developed to improve scatterometer wind retrievals at very high winds (Hersbach, 2003). Horstmann et al. (2005) tested the performance of this GMF at hurricane wind speeds retrieved from SAR and found it more suitable than CMOD4, as it copes better with saturation of NRCS at high winds. Figure 1 shows the relationship of NRCS to wind speed for CMOD-IFR2, CMOD4, and CMOD5. At moderate wind speeds (< 15 m s^{-1}), a given NRCS may translate to wind speeds differing by more than 1 m s^{-1} for the three GMFs. Such differences are significant in terms of wind power prediction. It is thus important to determine the optimal choice of GMF for accurate SAR wind retrievals.

Validation studies of SAR-retrieved winds against scatterometer measurements cannot reveal the GMF accuracy, as the scatterometer winds are retrieved from similar GMFs. In situ measurements from buoys and ships may be distorted due to blockage or motion of the sensor (Brown, 2000b). Ideally, SAR winds should be validated against in situ measurements from a mast with minimum flow distortion. High-quality meteorological measurements are obtained at most offshore wind farm sites. However, validation

studies based on such measurements are rare, as meteorological data from wind farm sites are often confidential.

In this paper, we validate wind speeds retrieved from a series of C-band satellite SAR images against in situ measurements obtained from an offshore meteorological mast at Horns Rev in the North Sea. SAR winds are retrieved from the geophysical model functions CMOD-IFR2, CMOD4, and CMOD5 using wind directions obtained from in situ measurements and image streaks, respectively. The latter encompasses the local gradient method of Koch (2004). Careful consideration is necessary, as satellite snapshots are compared to in situ measurements averaged over time. Conceptually, scalar footprint averaging is the correct approach (Hasager et al., 2004; Nielsen et al., 2004). We also test a simple box averaging method for extraction of SAR winds from the area surrounding the meteorological mast at Horns Rev.

The study site is located 14-21 km offshore and 2 km from a large offshore wind farm. SAR and in situ observations may thus be affected by internal boundary layers from the land (Garrat, 1990), interplaying with atmospheric stability effects (Stull, 1991). In addition, wind farm wake effects may impact our results (Christiansen & Hasager, 2005; 2006). The influence of these atmospheric parameters on SAR wind retrievals is quantified. Our systematic analysis aims to reveal the optimum method of SAR wind retrieval for wind power prediction. Finally, we discuss the concept of wind resource assessment from SAR images in proportion to traditional assessments from time series of meteorological measurements. Our findings could be valuable for those who wish to include satellite images in offshore wind resource assessment studies.

2. Data analysis

The offshore site Horns Rev in the North Sea (Figure 2) has been subject to intensive studies since 1998 when it was decided to build the world's first large scale offshore wind farm there. An offshore meteorological mast was erected in 1999. The wind farm, consisting of 80 turbines, became operational in December 2002. We have collected 97 ERS-2 and Envisat SAR images from Horns Rev over the period 1999-2005. Envisat scenes acquired in WSM mode cover 400 km x 400 km with a spatial resolution of ~100 m. All other scenes cover approximately 100 km x 100 km with a spatial resolution of ~30 m (Attema et al., 2000).

2.1. SAR wind retrieval

Winds were retrieved from the SAR images with the operational tool WiSAR developed at GKSS Research Center, Germany. The tool handles calibration to NRCS, wind direction retrieval using the local gradient (LG) method, and wind speed retrieval with CMOD-IFR2, CMOD4, and CMOD5. To retrieve wind directions, the 97 SAR images were divided into 10 km grid cells. Within each grid cell, local gradients of NRCS were computed at the scales 100 m, 200 m, and 400 m. Wind directions were assumed to be perpendicular to the local gradient of NRCS, especially at the smaller scales. Land was masked out of the images, as were other image features causing local gradients too steep to be associated with the wind. Examples of such features include wind turbines, ships, surfactants, and bathymetry. Several wind directions were typically suggested by the program for each grid cell. This was due to a 180° ambiguity and because a solution

was given for each scale. The appropriate wind direction input was selected manually according to streaks and wind shadows visible in the images. A second selection of wind directions was made automatically through comparison with model data. For the period 1999-2003, re-analysis data (ReMo) were available for the comparison. For 2004-2005, atmospheric model data provided by the German Weather Service (DWD) were used. The model data had a 6-hour temporal resolution.

For wind speed retrievals, the original NRCS images were reduced to eliminate effects of speckle noise and longer period waves on the wind retrievals. We chose a pixel size of 500 m as recommended by Horstmann et al. (2000). The LG wind directions, found through supervised and automatic image analysis, respectively, were re-sampled to match the NRCS images. The model functions CMOD-IFR2, CMOD4, and CMOD5 were run for each image with the two types of wind direction input. In addition, the model functions were run using wind directions from the meteorological mast at Horns Rev as input (see section 2.2 for details). The end result was nine different estimates of wind speed per pixel in the SAR images.

2.2. In situ measurements

The meteorological mast at Horns Rev is 62 m tall and operated by Elsam A/S. Wind speed (15, 30, 45, and 60 m), wind direction (62 m), and air temperature (13 and 55 m) are sampled at 1Hz and stored as 10-minute mean values. The error on measured wind speeds is <0.1 m s^{-1}. Wind speed at the three lower levels is measured simultaneously at both ends of a boom with the alignment 45°/225°. Wind shadowing from the mast was avoided by consequently selecting the upwind anemometer. No correction for

atmospheric stability or tidal sea level variations was made. The effect of such corrections has previously been found negligible for the site (Hasager et al., 2004). In situ measurements were averaged over one hour centred at the time of each satellite overpass to eliminate short-term fluctuations in the wind. The logarithmic velocity profile e.g. Stull (1991) was used to compute wind speeds at 10 m, corresponding to the SAR-retrieved winds. Practically, the logarithmic measurement heights were plotted as a function of wind speed and a linear fit was made. The 10 m wind speed was then extracted.

To determine the atmospheric stability at the acquisition time of each SAR scene, we computed the bulk Richardson number, Ri_B from wind speed and air temperature gradients measured at the meteorological mast:

$$Ri_B = \frac{g}{T} \frac{(\theta(z_1) - \theta(z_2)) / (z_1 - z_2)}{((u(z_3) - u(z_4)) / (z_3 - z_4))^2} \quad (2)$$

where g [m s^{-2}] is the acceleration due to gravity, T [K] is absolute temperature at a given height (z_1 in our case) and θ [K] is potential temperature, which is derived from T using the adiabatic lapse rate (-0.01 K m^{-1}). The measurement heights were z_1 = 55 m, z_2 = 13 m, z_3 = 62 m, and z_4 = 15 m. Estimates of atmospheric stability were valid at 55 m. The following intervals were defined: $Ri_B < -0.4$ for unstable atmospheres, $-0.4 \leq Ri_B \leq 0.1$ for near-neutral atmospheres, and $Ri_B > 0.1$ for stable atmospheres.

2.3. Comparison of SAR and in situ wind fields

SAR-retrieved wind fields were compared to measurements from the meteorological mast at Horns Rev using a scalar footprint approach. A scalar footprint is a response function based on dispersion theory, which quantifies the relative significance of distributed surface conditions at an elevated point in the atmospheric boundary layer. The weighted footprint of (Gash, 1986) was used to define the effective fetch, X_F [m] upstream of the meteorological mast:

$$X_F = -\frac{z\left(\ln\left(\frac{z}{z_0}\right) - 1 + \frac{z_0}{z}\right)}{\kappa^2 \ln\left(\frac{F}{100}\right)} \tag{3}$$

where F [%] is the percentage effective fetch, z_0 [m] is the roughness length, z [m] is the measurement height, and κ is von Karman's constant. The footprint of Gash (1986) applies to neutral atmospheric conditions and is the preferred footprint when stability information is unavailable (Nielsen et al., 2004). The footprint theories by Hsieh et al. (2000) and Horst & Weil (1994) takes atmospheric stability into account, but they require temperature gradients, which generally are unavailable for remote sensing applications.

Eq. (3) defines the upwind variation of a cross-wind integrated footprint, and according to dispersion theory the cross-wind variation is equal to that of a spreading plume, i.e. with a Gaussian profile (Horst & Weil, 1994). The upwind development of the length scale of the cross-wind profile is predicted by the model of Gryning et al. (1987). For each SAR image, a response function was evaluated by the observed wind speed and

direction and used to calculate a weighted average of pixel values upstream the mast. For the measurement height 10 m, the 90% effective fetch was 2.3 km for $z_0 = 0.2$ mm.

In addition to footprint averaging, we used simple box averaging to obtain mean winds for the area surrounding the meteorological mast at Horns Rev. Pixels were averaged within a 5 km square box centered at the meteorological mast. In some cases, bathymetry effects were visible within the box. To eliminate these effects, box averaging was repeated using the mask that was defined during the computation of local gradients. The mask covered areas with a very large gradient of NRCS. Wind turbines generate direct scattering, which is not associated with the wind. To avoid any contribution from wind turbine scattering, a polygon mask was defined over the wind turbine array. Pixels located within the polygon were eliminated, both from the scalar footprint and the box averaging. The wind farm polygon and the box used for pixel averaging are seen in Figure 3.

2.4. Wind resource assessment

The Risø Wemsar Tool (RWT) has been developed for wind resource assessment based on SAR-retrieved wind maps. The principle is to combine multiple SAR wind maps for computation of wind statistics over an area of interest defined by the user. The computation follows state-of-the-art procedures of wind power prediction from the Wind Atlas Analysis and Application Program (WAsP, see www.wasp.dk). A Weibull fit, defined by a scale parameter (A) and a shape parameter (k), is made to frequency observations of wind speed (u):

$$f(u) = \frac{k}{A}\left(\frac{u}{A}\right)^{k-1} \exp\left(-\left(\frac{u}{A}\right)^{k}\right) \quad (4)$$

A further description of the Weibull distribution applied to wind resource assessment is given by Troen & Petersen (1989). SAR wind retrievals are valid at 2-24 m s^{-1}. However, to make a correct Weibull fit; all wind speeds that are likely to occur at a site must be represented. To overcome this problem, RWT features an opportunity to type in the number of samples deselected due to high or low wind speeds. These samples are then taken into account in the fitting. RWT computes the mean wind speed (U) and the power density (E), and users have the opportunity to implement ground truth data for comparison studies using various footprint methods e.g. Gash (1986). RWT requires input arrays of wind speed and direction and a header file containing geo-information. In our case, the nine different wind fields computed with WiSAR were analyzed for the parameters U, A, k, and for E assuming a constant air density of 1.23 kg m^{-3} (Eq. 1).

3. Results

3.1. Wind direction retrievals

Figure 3 shows an example of a SAR wind speed map. Streaks are visible in the image, indicating the wind direction. In addition, orthogonal internal waves are seen at the top left image corner. Arrows show the wind direction measured at the meteorological mast (white) and wind directions retrieved with the LG method for the automatic runs (black). The local gradients deviate by ~10° from the in situ measurements and the orientation of visible wind streaks in the example. However, they still give a good

approximation of the wind direction. The internal waves did not impact the LG retrievals.

Wind directions estimated from local gradients are plotted in Figure 4 against in situ wind directions for scenes with wind speeds above 5 m s^{-1}. At lower wind speeds, in situ measurements of the wind direction may not be accurate. The plots show that wind directions were distributed over the full spectrum of 0-360°. For the supervised runs, a standard deviation (SD) of 21° and a correlation coefficient (R^2) of 0.95 was found between the LG and in situ wind directions. For the fully automatic runs, SD was 33° and R^2 was 0.87. Manual supervision of the LG retrievals thus led to a gain of accuracy on the wind direction estimates. Three outliers are seen for the automatic LG retrieval (Figure 4b). Two were associated with a weather front in the SAR images, confusing the automatic wind vector retrieval. For the third sample, bathymetry was clearly visible in the SAR image, impacting both the manual and the automatic LG wind direction. Eliminating the three outliers resulted in an improvement of SD to ~18° for both types of LG retrieval.

Figure 5 summarizes the wind distributions found from in situ measurements and the two different LG wind direction retrievals. All three methods suggest that winds from the southeast were prevailing with contributions of 15-18%. Large contributions (> 10%) were also found from the south-westerly sectors. The in situ data showed a high frequency at 300° (13%), whereas both LG retrievals yielded large contributions at 330° (9-13%). Contributions from west were remarkably low in all three cases, compared to a longer time series of data from Horns Rev. Observations of the wind climate at the

meteorological mast for the period April 1999 to November 2002 have been published by Sommer (2003). For the 3.5 years of measurements, winds from the directions 210-300° show almost equal prevalence (~12%). A significant contribution (9%) is reported for the sector centred at 120°, which confirms that south-easterly directions are important at Horns Rev.

3.2. Wind speed retrievals

Table 1 shows results of correlation analyses between SAR-retrieved and in situ wind speeds. The matrix contains results for the three different wind direction inputs, the three geophysical model functions, and the three comparison methods used. Also contained is the estimated mean wind speed, the Weibull A and k parameters, and the power density (see section 3.7 for description).

Wind speeds retrieved from SAR with in situ wind direction inputs yielded the best correlation with in situ wind speeds. A SD of 1.11 m s^{-1} with $R^2 = 0.89$ was found for CMOD-IFR2 using the box averaging method. Only a slight improvement of SD was found when a mask was implemented during the box averaging. However, the bias changed from -0.27 to -0.36, indicating that bright pixels were removed by the mask. The scalar footprint averaging method led to a SD of 1.44 m s^{-1} with $R^2 = 0.83$. The reason for the lower accuracies found from footprint averaging may be that fewer samples were obtained within the footprint compared to the 5 km square box. Moreover, the relatively small amount of pixels located within the 10% effective fetch of the meteorological mast was weighed very high in our footprint analysis. To increase the size of the scalar footprints the analysis was repeated, changing the height (z) in Eq. (3)

to 30 m with all other parameters constant. This resulted in an effective fetch of 21 km (90%). Our results did not improve significantly with the increased fetch, presumably because the fetch was limited by the coastline or the image border in several cases.

Wind speeds retrieved from the model functions CMOD-IFR2, CMOD4, and CMOD5 with in situ wind direction inputs are plotted against in situ wind speeds in Figure 6. The results were obtained from the box averaging method but trends were similar for box averaging using a mask, and for the footprint averaging (Table 1). CMOD-IFR2 wind retrievals yielded the minimum SD (1.11 m s^{-1}) and the maximum R^2 (0.89). SD was higher for CMOD5 (1.34 m s^{-1}) than for CMOD4 (1.21 m s^{-1}) but CMOD4 wind retrievals were better correlated with the in situ measurements than CMOD5 retrievals. CMOD-IFR2 and CMOD4 wind retrievals were negatively biased, whereas the bias was negligible for the CMOD5 retrievals.

A noticeable difference in SAR-retrieved wind speeds from the three model functions occurred for two incidents with in situ wind speeds of ~15 m s^{-1} (Figure 6). One of these incidents showed a wind speed of ~22 m s^{-1} retrieved from CMOD5. This particular satellite scene was acquired with the SAR looking almost directly into the wind. As seen from Figure 1, CMOD5 wind speed retrievals deviate from those of CMOD-IFR2 and CMOD4 for wind speeds > 15 m s^{-1}, looking upwind. A small increase of NRCS may lead to a very large increase of the predicted wind speed from CMOD5. In our correlation analysis, the wind speed retrieved with CMOD5 for one satellite scene contributed largely to the standard deviation found for this model function. Eliminating

the outlier improved the SD of CMOD5 to 1.13 m s^{-1} (i.e. nearly equal to CMOD-IFR2 retrievals but without a bias).

The standard deviation of SAR-retrieved wind speeds increased when wind directions were obtained from LG image analysis instead of in situ measurements. The minimum SD on wind speed, found using wind direction inputs from the supervised LG method, was 1.26 m s^{-1} with R^2=0.83. The corresponding SD found using wind direction inputs retrieved automatically was 1.51 m s^{-1} with R^2=0.77. In the following, we investigate the effect of internal boundary layers, atmospheric stability and wind farm wakes for SAR scenes acquired with a wind speed > 2 m s^{-1}. We also compare wind retrievals for SAR scenes with the spatial resolution ~30 m and ~100 m to determine how the choice of raw data impacts SAR wind retrievals.

3.3. Internal boundary layer effects

To quantify possible effects of internal boundary layers from the land, SAR scenes acquired with offshore winds were separated from scenes acquired with onshore winds. The Danish coastline facing the North Sea is aligned approximately from north to south. Wind directions ranging 0-180° from north were considered offshore and directions ranging 180-360° from north were considered onshore. A total of 49 SAR scenes appeared in the onshore bin, whereas 42 scenes appeared in the offshore bin. Computation of wind statistics was performed separately on the offshore and onshore data bins. As seen from Table 2, SD and R^2 were almost equal for the two bins, which suggests that scenes acquired with onshore and offshore winds were equally valid for the wind resource assessment study at Horns Rev. The bias, in contrast, was -0.52 m s^{-1}

for offshore winds and only -0.06 m s^{-1} for onshore winds. This indicates that bias associated with our SAR wind retrievals may originate partly from internal boundary layers due to the proximity of land.

3.4. Atmospheric stability effects

According to the bulk Richardson number (Ri_B), unstable atmospheric conditions occurred for 57% of the cases studied, whereas near-neutral and stable cases represented 24% and 19%, respectively. The SAR scenes were binned according to these intervals and comparisons of the SAR-derived and in situ wind speeds were made for each bin. Table 2 shows that the SD found for near-neutral stability (0.95 m s^{-1}) was lower than SD found for unstable (1.06 m s^{-1}) and stable (1.47 m s^{-1}) conditions. R^2 was 0.93 for near-neutral stability, which was higher than for any other selection of SAR scenes.

Scenes with stable conditions showed a relatively large negative bias (-0.86 m s^{-1}). The bias may result from a low wind stress at the sea surface, which is characteristic for highly stratified atmospheric boundary layers. Wind speeds from SAR were thus underestimated relative to the true 10-meter wind speeds measured at the mast. Similar results have been found from real aperture radar measurements by Dankert et al. (2003). Unstable conditions showed a smaller negative bias (-0.26 m s^{-1}). Normally, a high degree of atmospheric mixing compared to neutral conditions would lead to an overestimation of the wind speed at a given height according to the logarithmic profile law. In our case, unstable atmospheric conditions may have affected both the extrapolation of in situ measurements down to 10 m and the SAR wind retrievals. The

small negative bias found here may also result from parameters other than atmospheric stability.

Figure 7 illustrates the coupling between atmospheric stability, wind speed, and fetch length, as obtained from our dataset. Very stable and unstable conditions occurred at relatively low wind speeds in line with measurements from other meteorological stations in Denmark (Motta et al., 2005). The most extreme values of Ri_B, both for stable and unstable conditions, were found for offshore winds. Of the samples acquired with onshore winds, 66% showed near-neutral atmospheric conditions.

3.5. Wind farm wake effects

The meteorological mast is located 2 km from the wind farm at Horns Rev. It is thus possible that both SAR and in situ measurements experienced some influence of the wind farm in situations when the mast was located downwind of the wind turbines. A total of 46 SAR scenes were acquired before the wind farm at Horns Rev became operational in December 2002. This group of scenes was validated against in situ measurements, as was the group of 45 scenes acquired with turbines in operation. Table 2 shows an increase of SD from 0.93 to 1.20 m s^{-1} and a slight decrease of R^2 after the wind farm was build. To determine the effect of wind wakes further, 27 situations where the meteorological mast was located downwind of the wind farm were analyzed separately. The criteria for selecting the scenes were that the wind farm was installed and that the wind direction was within 90-270°. A SD of ~1.1 m s^{-1} and an R^2 of 0.89 was found, both for the wake scenes and for the rest of our dataset. We can therefore consider the impact of wake effects negligible in our comparison of SAR and in situ

winds. Wake effects may be reflected in the change of bias from -0.57 to 0.06 m s^{-1} after the wind farm installation. Direct scattering from the wind turbines did not impact our results, as the wind farm area was eliminated in the SAR images through masking.

3.6. Effects of spatial resolution

To test the importance of spatial resolution in the SAR images for accurate wind retrievals, correlation analyses were carried out for the SAR images with a ~30 m and a ~100 m spatial resolution, separately. The resolutions apply to the raw SAR data. Table 2 shows a small improvement of SD and R^2 for the scenes with a ~30 m resolution alone. Note that only 15 scenes were acquired with the ~100 m resolution, thus the two data types were not equally represented.

3.7. The wind resource

The mean wind speed (U) computed from in situ measurements at Horns Rev was 7.6 m s^{-1}, leading to a mean power density (E) of 422 W m^{-2} for our 97 samples (Table 2). Weibull fitting to the data gave the scale parameter A=8.5 m s^{-1} and the shape parameter k=2.5. Mean wind speeds were most accurately determined from SAR when the bias between in situ and SAR measurements was numerically small. Using in situ wind directions in combination with CMOD5 led to a mean wind speed identical to the in situ measurement. Results based on CMOD-IFR2 and CMOD4 showed under-predictions of U down to -6% and -14%, respectively.

Estimated power densities from SAR were generally most accurate where SD was small. Wind directions from the meteorological mast in combination with CMOD-IFR2

yielded a very good agreement on E with the in situ measurements; an E of 421 W/m^2 was found from box averaging. E was under-estimated down to -29% for the CMOD4 retrievals and over-estimated up to 27% for the CMOD5 retrievals. Estimates of E based on LG wind directions were possible to an accuracy of 17% for the supervised run and 21% for the automatic run, using CMOD-IFR2 and box averaging.

Figure 8 shows the frequency distribution of in situ and SAR wind speeds found from our 97 samples. Also shown is the Weibull fit to the data. The Weibull A parameter is proportional to U, therefore the best approximations of occurred with the best estimates of U from the SAR data. The Weibull k parameter found from the SAR wind fields was always lower than k from the in situ measurements, as k varied within the range 1.9-2.3.

4. Discussion

The aim of our study was to find the optimum method of SAR wind retrieval for wind resource assessment. The best approximation of SAR wind fields to in situ measurements was achieved using in situ wind direction inputs to feed the GMFs. Of the three GMFs validated at moderate wind speeds (2-15 m s^{-1}), CMOD-IFR2 yielded the lowest SD and the best correlation. However, a negative bias was found for this GMF in line with previous studies by Horstmann et al. (2002b), who concluded that CMOD-IFR2 is not completely suited to fetch limited conditions. CMOD4 retrievals showed a larger negative bias in our study, whereas the bias on CMOD5 retrievals was negligible.

Our analysis reveals that the method used to compare spatial means of SAR winds to temporal means of in situ measurements impacts correlation analyses. Simple averaging of pixels in the SAR images led to better agreement between SAR and in situ measurements of wind speed than the scalar footprint approach. The same conclusion was previously drawn by Hasager et al. (2004). Scalar footprint averaging of pixels in the SAR wind maps is based on atmospheric physics. A shortcoming of the method may be that too few pixels were averaged within the scalar footprint, leading to a higher noise level than for simple pixel averaging. Work is ongoing to adjust the width of scalar footprints used in RWT, in agreement with laws of atmospheric physics, to ensure that a sufficient number of SAR samples are included.

In situ measurements of the wind direction are not always available during the initial phase of planning an offshore wind farm, therefore the opportunity of estimating the wind direction from streaks in the SAR images was attractive. Detection of the wind direction from local gradients was possible to a SD of 21° when wind directions were selected manually amongst suggestions provided by the WiSAR program. Fully automatic retrievals using model data to select the appropriate direction yielded a larger SD. Wind speed retrievals based on the SAR wind directions were accurate to a SD of ~1.3 m s^{-1}, using manual supervision. A lot was gained on the wind speed accuracy, as LG wind direction retrievals were manually assisted; therefore we recommend this method to the fully automatic directional retrievals. The main reason for deviations of the automatic LG retrievals from the manually assisted retrievals was that interpolation was necessary between 6-hourly model runs used to resolve LG ambiguities. The model wind directions failed to give accurate directions in situations when a rapid change of

the wind field occurred (e.g. during a front passage). Further, the model resolution in space was coarser than the SAR resolution. In contrast to the in situ measurements, LG wind vectors had the advantage of showing spatial variability of the wind direction. At Horns Rev, this variability was limited. For other sites, variations may occur, as the wind is directed around topographical features such as mountains or islands. Examples of such variations in the form of gap flows and barrier jets have been given by Young & Winstead (2005).

Winds from offshore directions showed the best agreement on wind speed between SAR and in situ measurements, due to a long fetch. An improvement of SD was also found for cases with near-neutral atmospheric stability. This was expected, as the GMFs used for SAR wind retrievals are developed for open seas with a neutral atmosphere. Note that the empirical GMFs used for SAR wind retrievals are based on comparisons of NRCS to wind speed measurement from buoys and ships, usually without any correction for atmospheric stability (Brown, 2000a). Uncertainties related to offshore in situ measurements and stability effects are thus inherent.

Meteorological time series from offshore masts in Denmark show strong variations in the stability distribution from station to station with stable or unstable conditions up to 50% of the time (Motta et al., 2005). The frequent occurrence of unstable conditions found here (57%) is therefore realistic, especially because the prevailing wind direction in our dataset was southeast (i.e. from the land). Unstable conditions are normally associated with buoyancy effects generated through heating of air parcels over land. We have investigated SAR scenes acquired at low to moderate wind speeds (<15 m s^{-1}).

Stable and unstable atmospheric conditions occurred mainly at low wind speeds; therefore a relatively large impact of atmospheric stability effects was to be expected. Stability correction offshore is a notorious problem (e.g. Lange et al. (2004)).

Satellite scenes acquired before the wind farm at Horns Rev became operational showed an improved accuracy on wind speed retrievals compared to the entire dataset. However, a further analysis of scenes obtained when the meteorological mast at Horns Rev was located in the wind farm wake revealed very similar accuracies in terms of SD and R^2 for the wake and non-wake samples. Christiansen & Hasager (2005; 2006) have shown that reductions of the mean wind speed are detectable in SAR images up to 20 km downstream of large offshore wind farms. In the present study, it is likely that nearly identical wake impacts were observed from the SAR and in situ measurements.

None of the data bins investigated here showed errors large enough to justify elimination from our wind resource assessment. Instead, we recommend that the number of randomly selected samples is kept as high as possible in this type of study. The number of samples necessary for accurate wind resource assessment to an uncertainty of ±10% at the 90% confidence interval has previously been estimated (Barthelmie & Pryor, 2003; Pryor et al., 2004). To determine U and the Weibull A parameter, a total of 60-70 randomly selected samples are needed. Assessment of the Weibull k parameter and E requires a total of ~2000 samples. Satellite scenes are not acquired randomly in time. However, diurnal variation of the wind appears to be limited offshore and seasonal variability may be accounted for by selection of SAR scenes throughout the year.

The wind resource assessment presented here was based on 97 SAR scenes. We can thus consider our estimates of U and A robust. Wind statistics based on 3.5 years of data from the meteorological mast at Horns Rev have been reported by Sommer (2003). Extrapolation of the mean velocity profile down to 10 m leads to a U of ~7.6 m s^{-1}, which corresponds exactly to our prediction. A longer time series of data is available from a light ship, which was operating at Horns Rev in the period 1962-80 (Troen & Petersen, 1989). From this data series, U at 10 m is 7.3 m s^{-1}. Wind speeds exceeding 15 m s^{-1} were not represented in our dataset, although they do occur at the site studied. This may be the reason for our under-prediction of U relative to the longer time series of data. From the same time series, E is 456 W/m^2, and the Weibull parameters are A=8.3 m s^{-1}, and k=2.0 for roughness class 0 corresponding to oceans. The data are in very good agreement with our findings (Table 1), even though our dataset is too small for robust estimates of Weibull k and E. Obtaining a total of ~2000 SAR scenes for more robust wind power predictions is realistic as the cost of purchasing satellite data is currently decreasing. On the other hand, a lot of information about the wind resource may be gained from relatively few well-distributed SAR samples, simply by studying the spatial variability of the mean wind speed (e.g. Schneiderhan et al. (2005)).

The results presented here are valid at 10 m. Projecting the power predictions to a higher level (i.e. turbine hub height) is attractive for wind farm developers and possible in RWT. However, some additional error may be introduced due to necessary assumptions about the logarithmic profile law and the sea surface roughness. Finally, weighting of the wind energy contribution from different wind sectors may be useful in

situations when the prevailing wind direction found from SAR samples and meteorological time series measurements differ (Choisnard et al., 2004). Further investigation of this approach is needed.

5. Conclusion

Our systematic analysis shows that it is possible to estimate the wind resource accurately from a series of SAR images. The accuracy of mean wind speeds was determined by the bias on SAR wind retrievals. The accuracy on power prediction, in contrast, was determined by the standard deviation of SAR winds relative to ground truth data. The best approximation of SAR winds to offshore in situ measurements at Horns Rev was obtained from the model function CMOD-IFR2, using in situ wind directions as input (SD ~ 1.1 m s^{-1}, $R^2 = 0.89$). Satisfactory results were also achieved using wind directions obtained from local gradients in the SAR images, independently of in situ measurements (SD ~ 1.3 m s^{-1}, $R^2 = 0.83$). A negative bias was found for wind retrievals with CMOD-IFR2 and CMOD4, whereas CMOD5 retrievals were bias-free. The mean wind speed and power density found for a series of 97 randomly selected SAR scenes compared well to results obtained from in situ measurements, both for the SAR data acquisition times and for longer time series of in situ data. We therefore conclude that SAR images are valuable in offshore wind resource assessment, as they provide spatial information at an absolute accuracy sufficient in the early stage of wind farm planning. The absolute accuracy on SAR-based wind power prediction may improve in the future, as more SAR scenes are made available at a lower cost.

Acknowledgements

The work presented here was funded by Risø National Laboratory and the Danish Research Agency through the SAT-WIND project (2058-03-0006). Satellite scenes were provided by the European Space Agency through the Cat. 1 project EO-1356. Elsam A/S kindly provided in situ measurements from the mast at Horns Rev. Model data were made available by the German Weather Service (DWD) and GKSS Research Centre.

References

Attema, E., Desnos, Y.-L., & Duchossiois, G. (2000). Synthetic aperture radar in Europe: ERS, Envisat, and beyond. *The Johns Hopkins APL Technical Digest*, *21*, 155-169.

Barthelmie, R. J., & Pryor, S. C. (2003). Can satellite sampling of offshore wind speeds realistically represent wind speed distributions. *Journal of Applied Meteorology*, *42*, 83-94.

Brown, R. A. (2000a). On satellite scatterometer model functions. *Journal of Geophysical Research*, *105*, 29195-29205.

Brown, R. A. (2000b). Serendipity in the use of satellite scatterometer, SAR and other sensor data. *The Johns Hopkins APL Technical Digest*, *21*, 21-26.

Choisnard, J., Lafrance, G., & Bernier, M. (2004). SAR-satellite for offshore and coastal wind resource analysis, with examples from St. Lawrence Gulf, Canada. *Wind Engineering*, *28*, 367-382.

Christiansen, M. B., & Hasager, C. B. (2005). Wake effects of large offshore wind farms identified from satellite SAR. *Remote Sensing of Environment*, *98*, 251-268.

Christiansen, M. B., & Hasager, C. B. (2006). Using airborne and satellite SAR for wake mapping offshore. *Wind Energy*, *in press*.

Dankert, H., Horstmann, J., & Rosenthal, W. (2003). Ocean wind fields retrieved from radar-image sequences. *Journal of Geophysical Research - Oceans*, *108*.

Du, Y., Vachon, P. W., & Wolfe, J. (2002). Wind direction estimation from SAR images of the ocean using wavelet analysis. *Canadian Journal of Remote Sensing*, *28*, 498-509.

Fichaux, N., & Ranchin, T. (2002). Combined extraction of high spatial resolution wind speed and direction from SAR images: a new approach using wavelet transform. *Canadian Journal of Remote Sensing*, *28*, 510-516.

Furevik, B., Johannessen, O., & Sandvik, A. D. (2002). SAR-retrieved wind in polar regions - comparison with in situ data and atmospheric model output. *IEEE Transactions on Geoscience and Remote Sensing*, *40*, 1720-1732.

Garrat, J. R. (1990). The internal boundary layer - a review. *Boundary-Layer Meteorology*, *50*, 171-203.

Gash, J. H. C. (1986). A note on estimating the effect of a limited fetch on micrometeorological evaporation measurements. *Boundary-Layer Meteorology*, *35*, 409-413.

Gerling, T. W. (1986). Structure of the surface wind field from the SEASAT SAR. *Journal of Geophysical Research*, *91*, 2308-2320.

Gryning, S. E., Holtslag, A. A. M., Irvin, J. S., & Sivertsen, B. (1987). Applied dispersion modelling based on meteorological scaling parameters. *Atmospheric Environment*, *21*, 79-89.

Hasager, C. B., Dellwik, E., Nielsen, M., & Furevik, B. (2004). Validation of ERS-2 SAR offshore wind-speed maps in the North Sea. *International Journal of Remote Sensing*, *25*, 3817-3841.

Hasager, C. B., Nielsen, M., Astrup, P., Barthelmie, R. J., Dellwik, E., Jensen, N. O., Jørgensen, B. H., Pryor, S. C., Rathmann, O., & Furevik, B. (2005). Offshore wind resource estimation from satellite SAR wind field maps. *Wind Energy*, *8*, 403-419.

He, Y. J., Perrie, W., Zou, Q. P., & Vachon, P. W. (2005). A new wind vector algorithm for C-band SAR. *IEEE Transactions on Geoscience and Remote Sensing*, *43*, 1453-1458.

Hersbach, H. (2003). *CMOD5. An improved geophysical model function for ERS C-band scatterometry*. (pp. 1-50). Reading, UK: ECMWF Technical Memorandum 395.

Horst, T. W., & Weil, J. C. (1994). How far is far enough? - The fetch requirements for micrometeorological measurement of surface fluxes. *Journal of Atmospheric and Oceanic Technology*, *11*, 1018-1025.

Horstmann, J., Koch, W., Lehner, S., & Tonboe, R. (2002a). Ocean winds from RADARSAT-1 ScanSAR. *Canadian Journal of Remote Sensing*, *28*, 524-533.

Horstmann, J., Lehner, S., Koch, W., & Tonboe, R. (2000). Computation of wind vectors over the ocean using spaceborne syntheric aperture radar. *The Johns Hopkins APL Technical Digest*, *21*, 100-107.

Horstmann, J., Schiller, H., Schulz-Stellenfleth, J., & Lehner, S. (2003). Global wind speed retrieval from SAR. *IEEE Transactions on Geoscience and Remote Sensing*, *41*, 2277-2286.

Horstmann, J., Thompson, D. R., Monaldo, F., & Graber, H. C. (2005). Can synthetic aperture radars be used to estimate hurricane force wind fields? *Geophysical Research Letters*.

Horstmann, J., Weinreich, I., Hauser, D., Lehner, S., & Koch, W. (2002b). SAR wind measurements during the FETCH experiment. *Elsevier Oceanography Series*, *66*, 445-453.

Koch, W. (2004). Directional analysis of SAR images aiming at wind direction. *IEEE Transactions on Geoscience and Remote Sensing*, *42*, 702-710.

Lange, B., Larsen, S., Højstrup, J., & Barthelmie, R. (2004). The influence of thermal effects on the wind speed profile of the coastal marine boundary layer. *Boundary-Layer Meteorology*, *112*, 587-617.

Lehner, S., Horstmann, J., Koch, W., & Rosenthal, W. (1998). Mesoscale wind measurements using recalibrated ERS SAR images. *Journal of Geophysical Research - Oceans*, *103*, 7847-7856.

Monaldo, F. (2000). The Alaska SAR demonstration and near-real-time synthetic aperture radar winds. *The Johns Hopkins APL Technical Digest*, *21*, 75-79.

Monaldo, F., & Kerbaol, V. (2003). The SAR measurement of ocean winds: an overview for the 2nd workshop on coastal and marine applications of SAR. *Proceedings of the Second Workshop on Coastal and Marine Applications of SAR, 8-12 September 2003, Svalbard (N)*.

Monaldo, F. M., Thompson, D. R., Beal, R. C., Pichel, W. G., & Clemente-Colón, P. (2001). Comparison of SAR-derived wind speed with model predictions and ocean buoy measurements. *IEEE Transactions on Geoscience and Remote Sensing*, *39*, 2587-2600.

Monaldo, F. M., Thompson, D. R., Pichel, W. G., & Clemente-Colon, P. (2004). A systematic comparison of QuikSCAT and SAR ocean surface wind speeds. *IEEE Transactions on Geoscience and Remote Sensing*, *42*, 283-291.

Motta, M., Barthelmie, R. J., & Vølund, P. (2005). The influence of non-logarithmic wind speed profiles on potential power output at Danish offshore sites. *Wind Energy*, *8*, 219-236.

Nielsen, M., Astrup, P., Hasager, C. B., Barthelmie, R. J., & Pryor, S. C. (2004). *Satellite information for wind energy applications*. Risø-R-1479(EN) (pp. 1-57). Roskilde, Denmark: Risø National Laboratory.

Pryor, S. C., Nielsen, M., Barthelmie, R. J., & Mann, J. (2004). Can satellite sampling of offshore wind speeds realistically represent wind speed distributions? Part II: Quantifying uncertainties associated with sampling strategy and distribution fitting methods. *Journal of Applied Meteorology*, *43*, 739-750.

Quilfen, Y., Chapron, B., Elfouhaily, T., Katsaros, K., & Tournadre, J. (1998). Observation of tropical cyclones by high-resolution scatterometry. *Journal of Geophysical Research*, *103*, 7767-7786.

Schneiderhan, T., Lehner, S., Schulz-Stellenfleth, J., & Horstmann, J. (2005). Comparison of offshore wind park sites using SAR wind measurement techniques. *Meteorological Applications*, *12*, 101-110.

Sommer, A. (2003). Offshore measurements of wind and waves at Horns Rev and Laesoe, Denmark. *OWEMES, 10-12 April 2003, Naples (I)*, 65-79.

Stoffelen, A., & Anderson, D. L. T. (1997). Scatterometer data interpretation: Estimation and validation of the transfer fuction CMOD4. *Journal of Geophysical Research*, *102*, 5767-5780.

Stull, R. B. (1991). *An Introduction to Boundary Layer Meteorology*. (pp. 1-666). Dordrecht: Kluwer Academic Puhlishers.

Thompson, D., Elfouhaily, T., & Chapron, B. (1998). Polarization ratio for microwave backscattering from the ocean surface at low to moderate incidence angles. *Proceedings International Geoscience and Remote Sensing Symposium, Seattle, WA*, 1671-1676.

Troen, I., & Petersen, E. L. (1989). *European Wind Atlas*. (pp. 1-656). Roskilde: Risø National Laboratory.

Young, G., & Winstead, N. (2005). Meteorological phenomena in high resolution SAR wind imagery. In B.Beal, G.Young, F.Monaldo, D.Thompson, N.Winstead, & C.Scott (Eds.), *High Resolution Wind Monitoring with Wide Swath SAR: A User's Guide* (pp. 13-34). Washington, DC: U.S. Department of Commerce, National Oceanic and Atmospheric Administration.

Figure captions

Figure 1. Normalized radar cross section (NRCS) as a function of wind speed for the fixed radar incidence angle 40°. The relationship is plotted for three geophysical model functions (CMOD-IFR2, CMOD4, and CMOD5) with the SAR looking upwind and crosswind, respectively.

Figure 2. Map of Denmark showing the location of Horns Rev in the North Sea.

Figure 3. ERS-2 SAR wind field from 21 September 2000 at 21:30 UTC. At Horns Rev, the meteorological mast (star), the wind farm (trapezoid), and the 5 km square box used for pixel averaging are indicated. Arrows show the in situ wind direction (white) and the automatic local gradient wind vectors (black). Image streaks indicate the wind direction. and orthogonal internal waves are visible at the top left image corner.

Figure 4. In situ wind directions versus SAR wind directions retrieved with a) the supervised local gradient method, and b) the automatic local gradient method for wind speeds >5 m s^{-1}. In situ wind directions were measured at 62 m and averaged over one hour, centred at the SAR data acquisition times.

Figure 5. Directional distribution of winds at Horns Rev found from in situ measurements, the supervised, and the automatic local gradient method (LG). Frequencies are given in % and directions in degrees from North (N=91).

Figure 6. In situ wind speeds versus SAR wind speeds retrieved with a) CMOD-IFR2, b) CMOD4, and c) CMOD5. In situ measurements were extrapolated to the height 10 m and averaged over one hour, centred at the SAR data acquisition times. Comparisons with the SAR wind speed maps were made through box averaging.

Figure 7. In situ wind speed (15m) as a function of atmospheric stability, expressed by the bulk Richardson number, Ri_B. Intervals are defined as $Ri_B < -0.4$ for unstable atmospheres, $-0.4 \leq Ri_B \leq 0.1$ for near-neutral atmospheres, and $Ri_B > 0.1$ for stable atmospheres. Offshore winds (0-180°) and onshore winds (180-360°) are plotted separately.

Figure 8. Frequency distribution of wind speeds at 10 m and Weibull fits for a) in situ measurements, and b) SAR winds retrieved with CMOD-IFR2 and in situ wind directions. The lack of SAR winds <2 m s^{-1} was accounted for in the Weibull fitting (N=91).

Table captions

Table 1. Results of correlation analyses between SAR and in situ wind speeds: standard deviation (SD), bias, and correlation coefficient (R^2). Also listed are mean wind speeds (U), Weibull A and k parameters, and the mean power density (E) computed from Eq. (1) with an air density of 1.23 kg m^{-3} (N=91).

Table 2. Results of correlation analyses between SAR and in situ wind speeds found from CMOD-IFR2 wind retrieval and box averaging. The table shows the standard deviation (SD), bias, and correlation coefficient (R^2), and the number of samples (N) for various groupings of SAR scenes.

Figure 1

Click here to download high resolution image

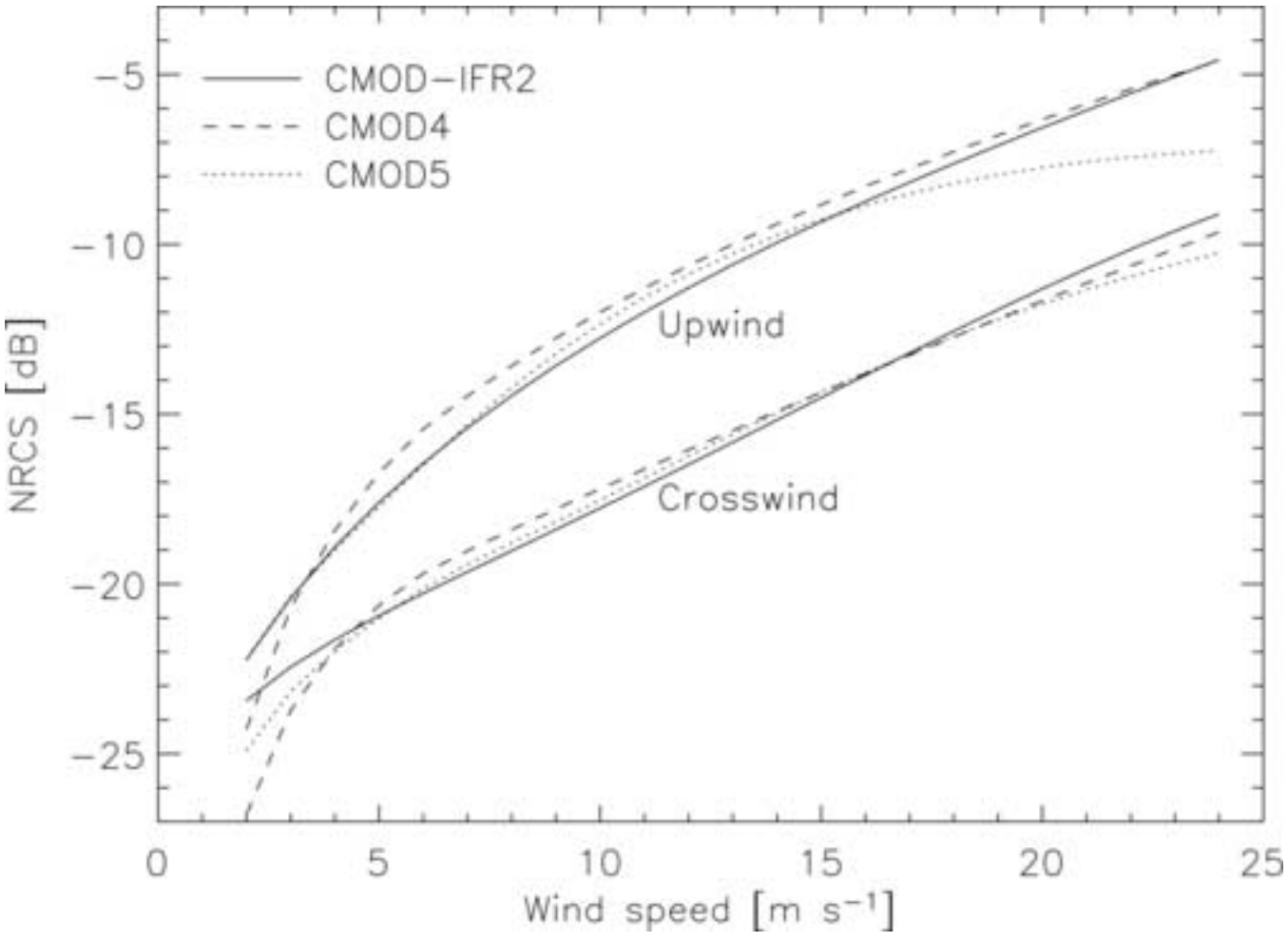

Figure 2

Click here to download high resolution image

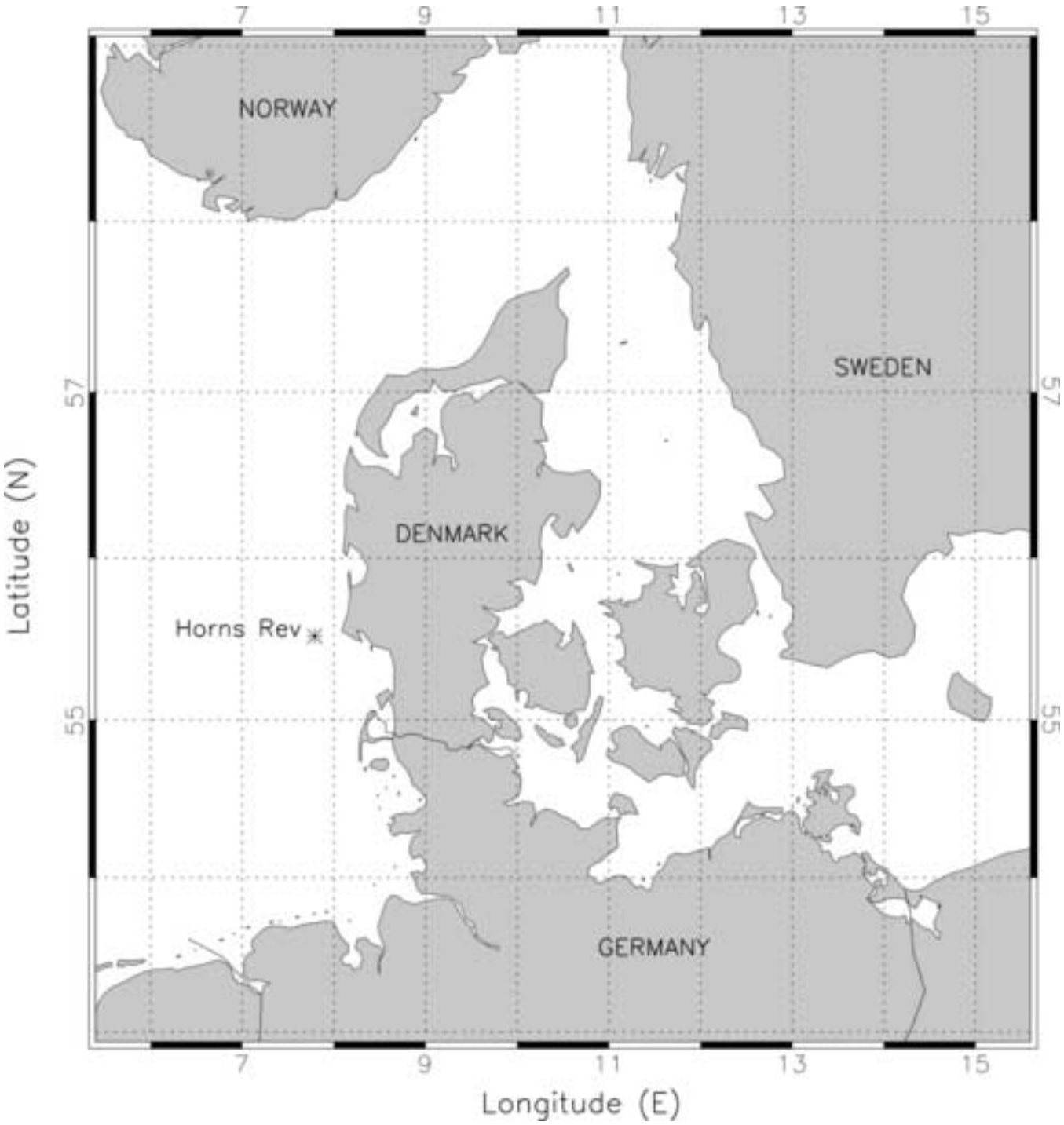

Figure 3

Click here to download high resolution image

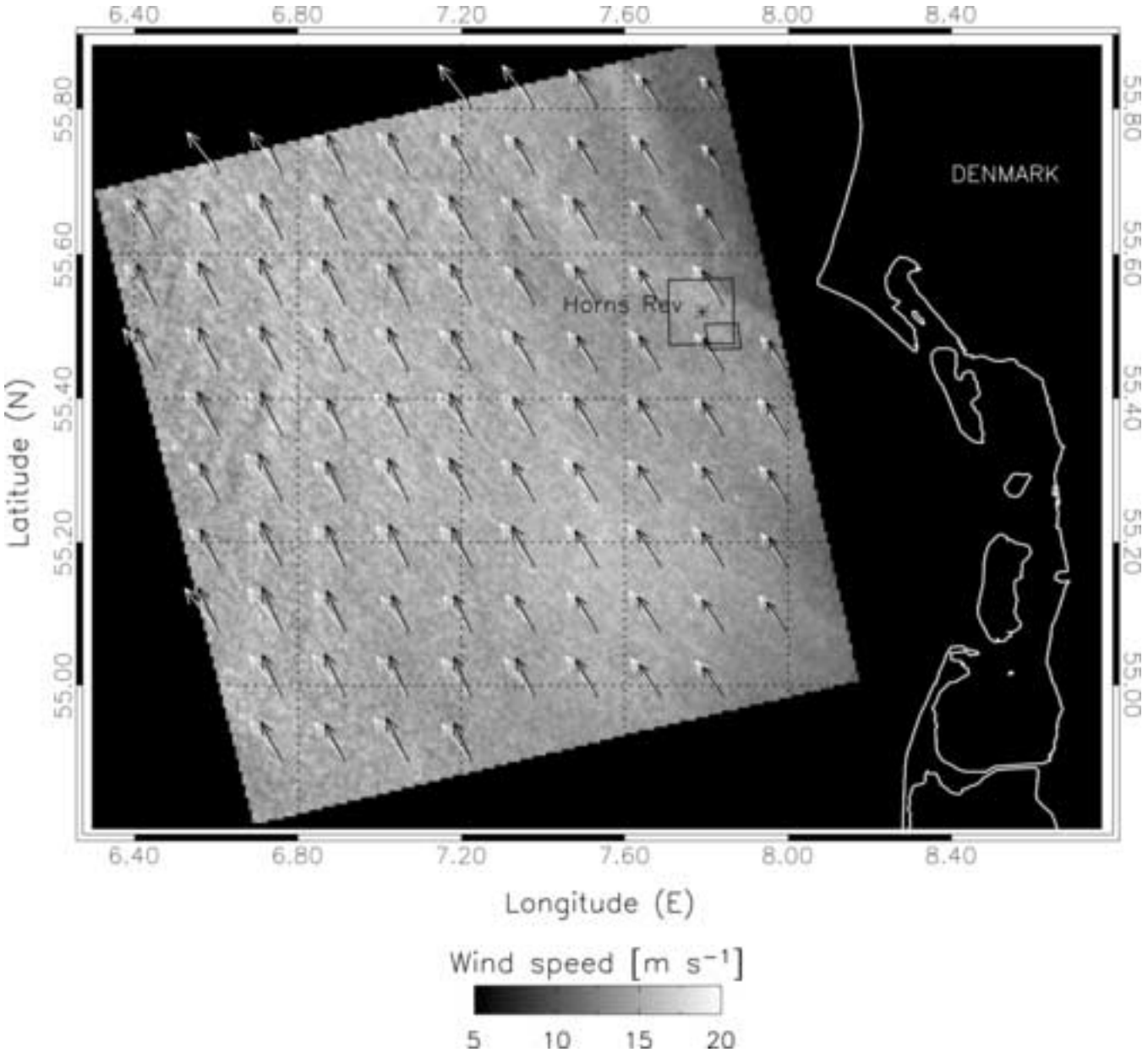

Figure 4a
Click here to download high resolution image

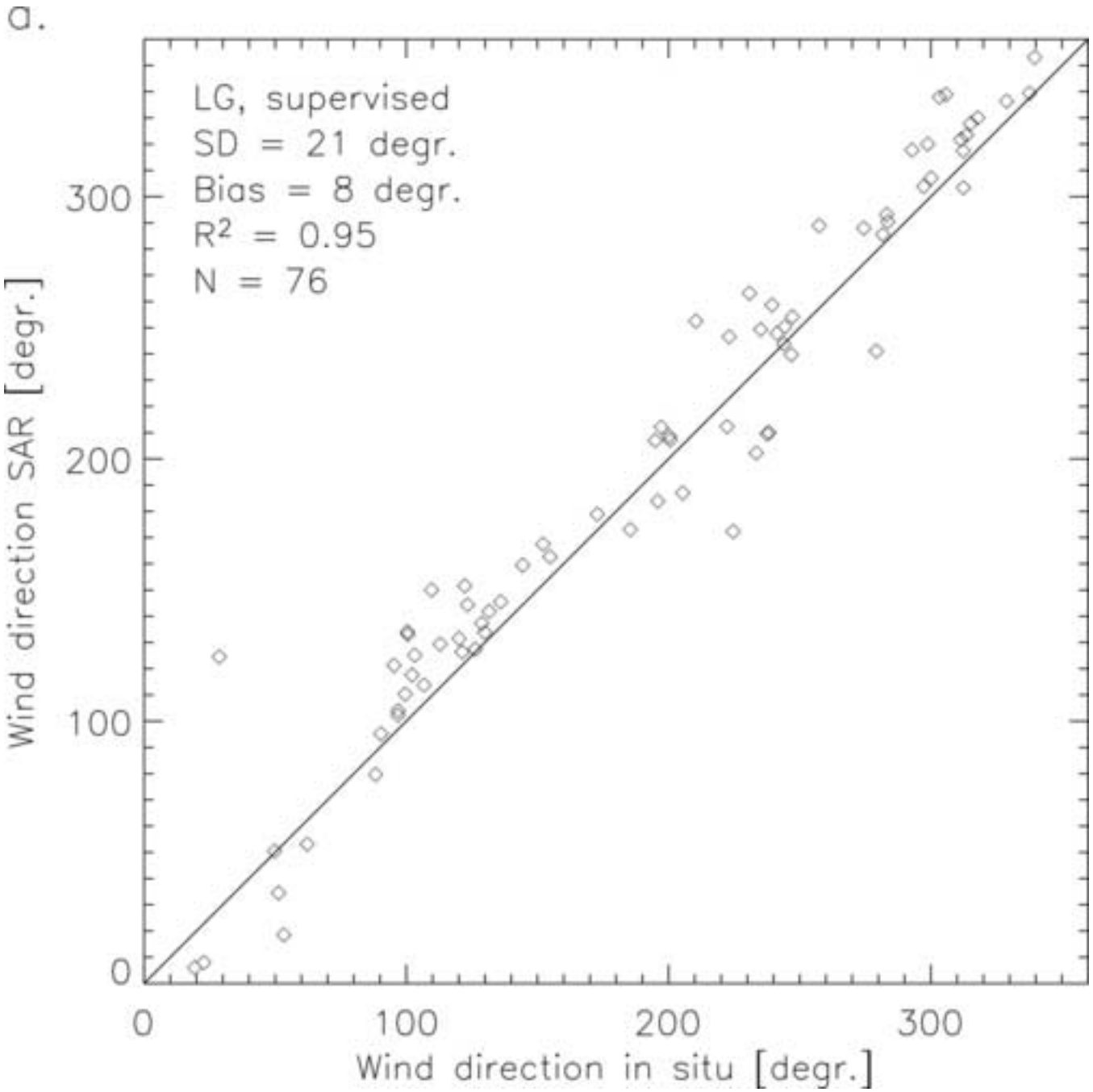

Figure 4b

Click here to download high resolution image

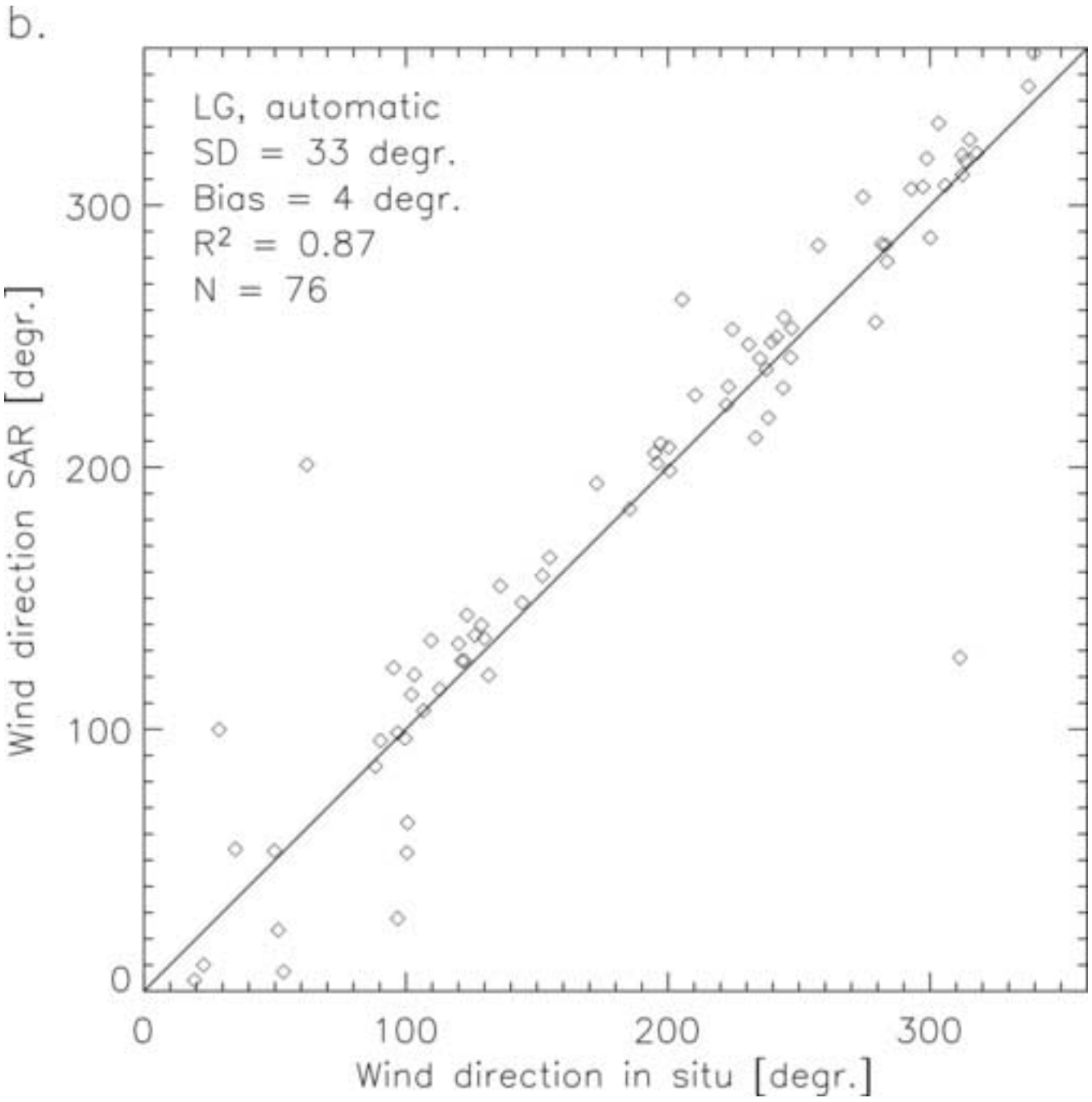

Figure 5

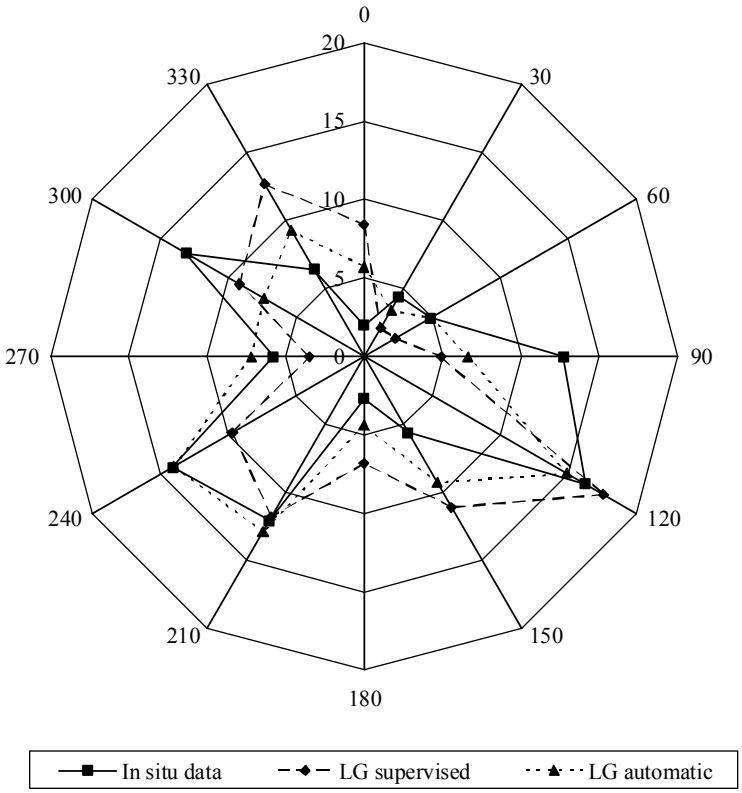
0
20
30
15
60
10
300
5
90
270
0
120
240
150
210
180
In situ data
LG supervised
LG automatic

Figure 6a
Click here to download high resolution image

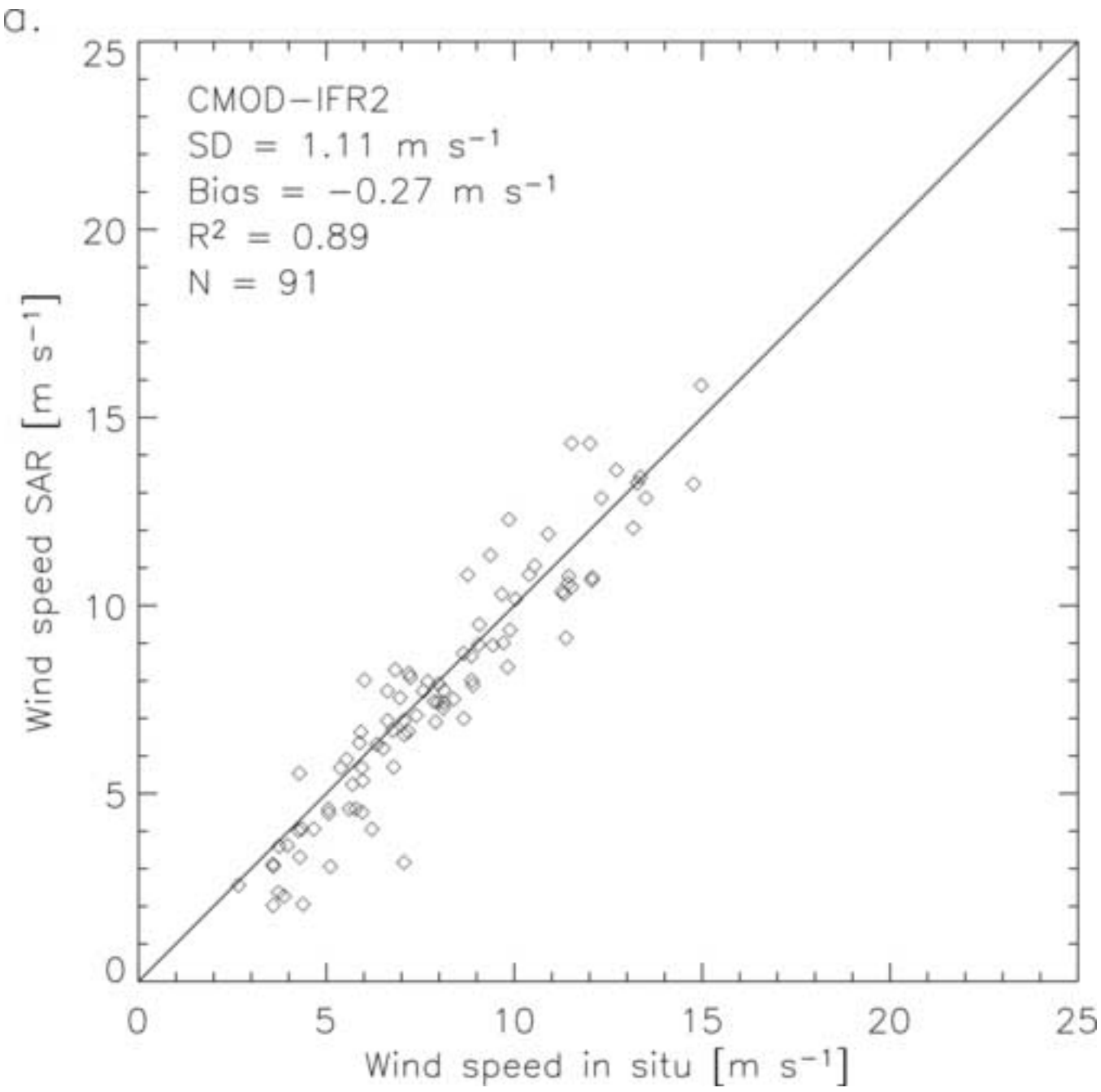

Figure 6b

Click here to download high resolution image

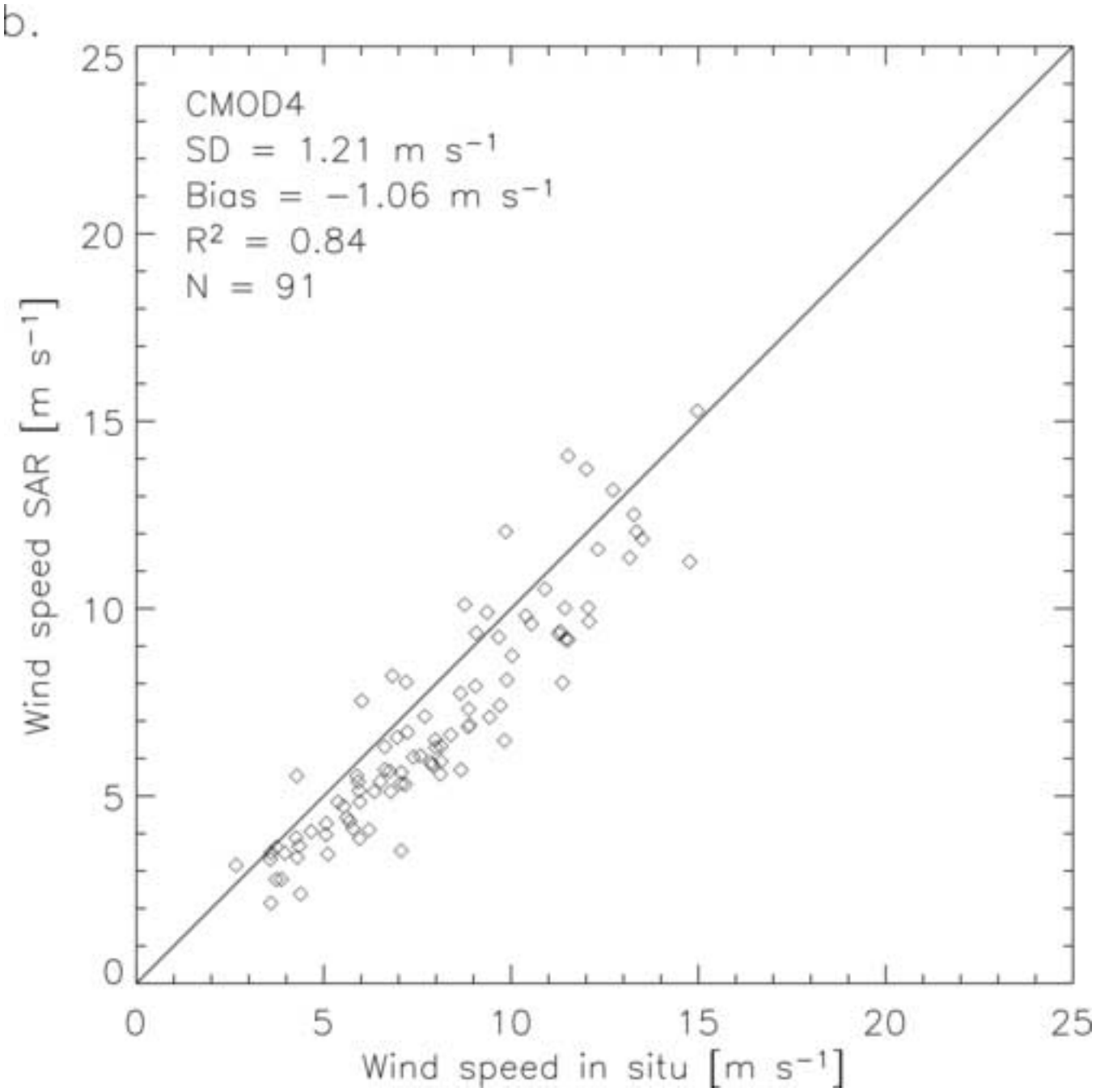

Figure 6c
Click here to download high resolution image

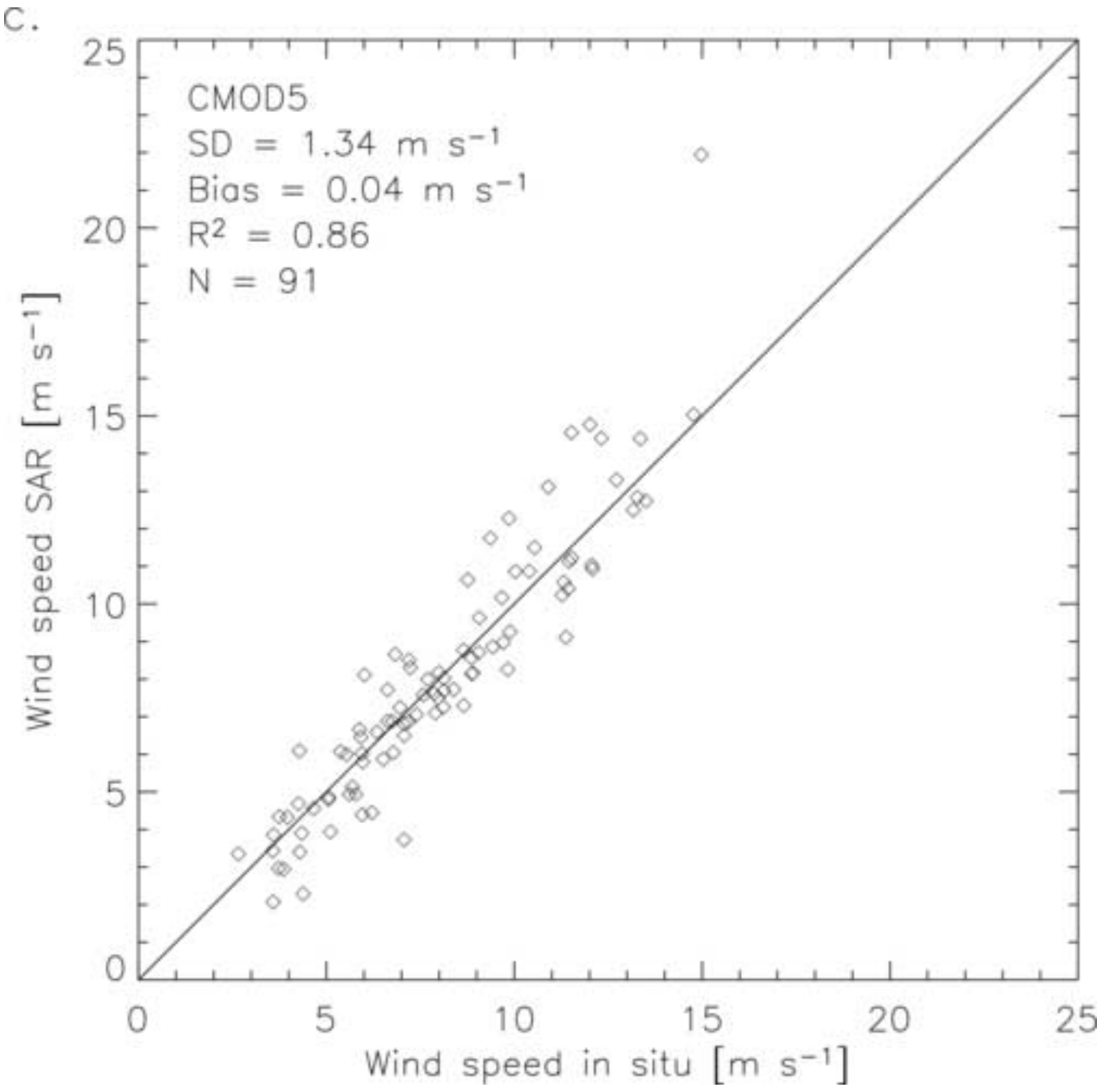

Figure 7

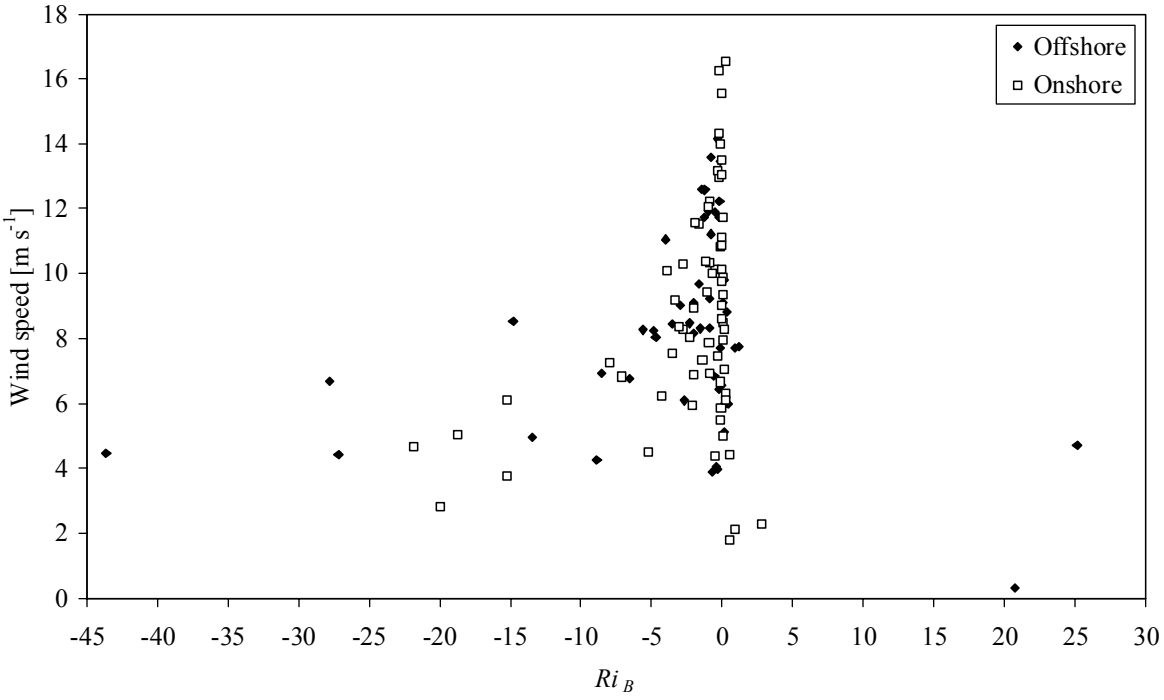
Offshore
Onshore
Wind speed [m s-1]
Ri B
18
16
14
12
10
8
6
4
2
0
-45
-40
-35
-30
-25
-20
-15
-10
-5
0
5
10
15
20
25
30

Figure 8

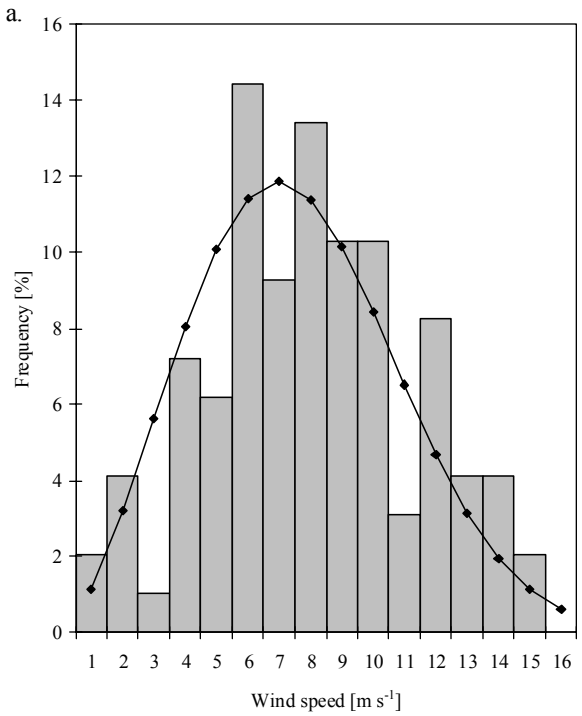
a.
Frequency [%]
0
2
4
6
8
10
12
14
16
1 2 3 4 5 6 7 8 9 10 11 12 13 14 15 16
Wind speed [m s-1]

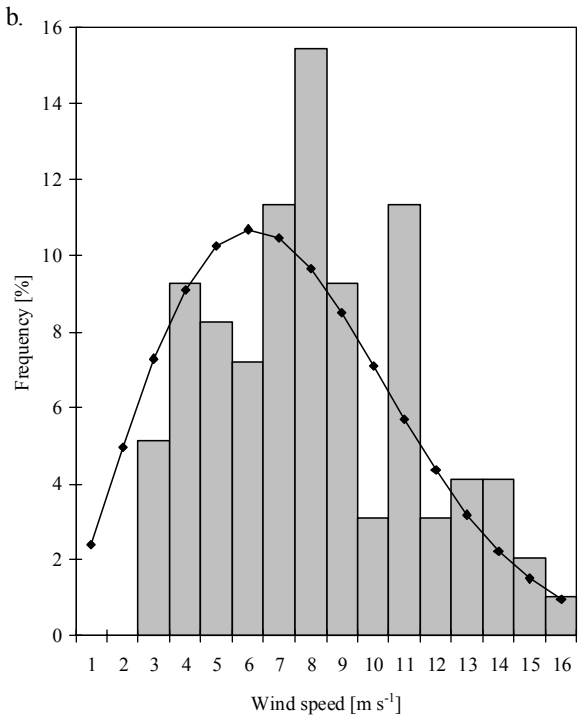
b.
Frequency [%]
0
2
4
6
8
10
12
14
16
1 2 3 4 5 6 7 8 9 10 11 12 13 14 15 16
Wind speed [m s-1]

Table 1

		Wind direction from mast						
		SD [m s^{-1}]	Bias [m s^{-1}]	R^2	U [m s^{-1}]	A [m s^{-1}]	k	E [W m^{-2}]
Box	CMOD-IFR2	1.11	-0.27	0.89	7.3	8.3	2.2	421
	CMOD4	1.21	-1.06	0.84	6.6	7.4	2.2	309
	CMOD5	1.34	0.04	0.86	7.6	8.6	2.1	487
Box, masked	CMOD-IFR2	1.09	-0.36	0.89	7.2	8.2	2.2	405
	CMOD4	1.20	-1.14	0.84	6.5	7.4	2.2	299
	CMOD5	1.33	-0.06	0.86	7.5	8.5	2.1	469
Footprint	CMOD-IFR2	1.44	-0.23	0.83	7.4	8.3	2.1	444
	CMOD4	1.51	-1.02	0.77	6.6	7.5	2.1	328
	CMOD5	1.81	0.13	0.78	7.7	8.7	2.0	535

		Wind direction from LG, supervised						
		SD [m s^{-1}]	Bias [m s^{-1}]	R^2	U [m s^{-1}]	A [m s^{-1}]	k	E [W m^{-2}]
Box	CMOD-IFR2	1.39	0.27	0.82	7.8	8.8	2.3	496
	CMOD4	1.27	-0.64	0.83	7.0	7.9	2.3	357
	CMOD5	1.50	0.50	0.83	8.0	9.1	2.2	555
Box, masked	CMOD-IFR2	1.36	0.16	0.83	7.7	8.7	2.3	476
	CMOD4	1.26	-0.74	0.83	6.9	7.8	2.3	343
	CMOD5	1.47	0.37	0.83	7.9	8.9	2.2	532
Footprint	CMOD-IFR2	1.62	0.23	0.79	7.8	8.8	2.2	511
	CMOD4	1.47	-0.68	0.79	7.0	7.9	2.2	365
	CMOD5	1.79	0.49	0.79	8.0	9.1	2.1	585

		Wind direction from LG, automatic						
		SD [m s^{-1}]	Bias [m s^{-1}]	R^2	U [m s^{-1}]	A [m s^{-1}]	k	E [W m^{-2}]
Box	CMOD-IFR2	1.73	0.18	0.76	7.7	8.7	2.1	510
	CMOD4	1.54	-0.74	0.77	6.9	7.8	2.1	362
	CMOD5	2.05	0.44	0.73	8.0	9.0	2.0	591
Box, masked	CMOD-IFR2	1.70	0.07	0.76	7.6	8.6	2.1	491
	CMOD4	1.51	-0.82	0.77	6.8	7.7	2.1	349
	CMOD5	2.02	0.33	0.73	7.9	8.9	2.0	568
Footprint	CMOD-IFR2	2.01	0.24	0.72	7.8	8.8	2.0	547
	CMOD4	1.76	-0.69	0.73	7.0	7.8	2.1	384
	CMOD5	2.42	0.55	0.68	8.1	9.1	1.9	653

					U [m s^{-1}]	A [m s^{-1}]	k	E [W m^{-2}]
In situ data		-	-	-	7.6	8.5	2.5	422

Table 2

	SD [m s^{-1}]	Bias [m s^{-1}]	R^2	N
Onshore winds	1.10	-0.06	0.89	49
Offshore winds	1.08	-0.52	0.88	42

	SD [m s^{-1}]	Bias [m s^{-1}]	R^2	N
Stable	1.47	-0.86	0.88	11
Near-neutral	0.95	-0.13	0.93	22
Unstable	1.06	-0.26	0.85	52

	SD [m s^{-1}]	Bias [m s^{-1}]	R^2	N
No wind farm	0.93	-0.57	0.90	46
Wind farm	1.20	0.04	0.87	45

	SD [m s^{-1}]	Bias [m s^{-1}]	R^2	N
Spatial resolution ~30 m	1.00	-0.46	0.90	76
Spatial resolution ~100 m	1.15	0.71	0.85	15